ORIGINAL RESEARCH PAPER

Local Fuel Starvation Degradation of an Automotive PEMFC Full Size Stack▲

M. Obermaier[1]*, M. Rauber[1], A. Bauer[1], T. Lochner[1], F. Du[1], C. Scheu[2,3]*

[1] BMW AG, Petuelring 130, 80788 München, Germany
[2] Max-Planck-Institut für Eisenforschung GmbH, Max-Planck-Str. 1, 40237 Düsseldorf, Germany
[3] Materials Analytics, RWTH Aachen University, Kopernikusstr. 10, 52074 Aachen, Germany

Abstract

The achievement of durability targets is an important challenge for the commercialization of fuel cell electric vehicles (FCEV). In order to meet the requirements, knowledge about the most severe degradation mechanisms of fuel cell stacks under automotive conditions is crucial. In the present work, degradation analysis of an automotive full size stack is performed. Herein, we focus on defects at the cathode catalyst layer and their interrelation including inhomogeneous adhesion of the microporous layer on the catalyst layer, crack formation, cathode catalyst layer thinning and wrinkling of the catalyst coated membrane. In addition, we report linear and circular Pt depositions on top of the cathode catalyst layer,

which have to the best of our knowledge not been described in literature yet. For the latter, a degradation mechanism based on liquid water formation, local fuel starvation and current density distribution at the interface between microporous layer and cathode catalyst layer is postulated. Finally, a fast indication for stack degradation is suggested by correlating different degradation phenomena. This improved stack analysis approach allowed us to detect local differences in degradation on both cell and stack level.

Keywords: Automotive Application, Catalyst Layer, Degradation, Durability, Fuel Cell, Hydrogen Car, MEA, PEMFC, PEM Fuel Cell System, Polymer Electrolyte Membrane Fuel Cell

1 Introduction

Electromobility is a key technology for reducing both greenhouse gas emission and urban air pollution in the mobility sector. Increasing traffic numbers [1] make the implementation of these goals even more challenging. Fuel cell electric vehicles allow both a high driving range and quick refueling time, while having zero emission and are thus considered a promising candidate for green mobility [2]. Fuel cell electric vehicles (FCEVs) generate power with the help of a fuel cell stack typically assembled from several hundreds of single polymer electrolyte membrane fuel cells (PEMFCs). A state-of-the-art PEMFC itself consists of various components including bipolar plates and a membrane electrode assembly (MEA). The latter has two gas diffusion layers (GDLs) and a catalyst coated membrane (CCM). The GDL typically consists of a substrate like carbon paper and a microporous layer (MPL). Catalyst coated membranes are composed of a proton con-

ducting membrane covered with two catalyst layers. For the commercialization of fuel cell electric vehicles a sufficient durability (>5,000 h) of the fuel cell stack is required [3]. Therefore, knowledge about full size stack degradation under realistic conditions is crucial. Several studies performed degradation analysis on lab-scale size single cells [4–7], on lab-scale short- and mid-size-stacks [8–12] as well as on automotive size single cells [13] and on automotive size short- and midsize-stacks [14–16]. However, only few studies exist which analyze the degradation of automotive full size stacks (>350 cells, active area approx. 300 cm²). For instance, Ettingshausen et al. [17] and Pei et al. [18] investigated a full size stack of a prototype vehicle and a full size stack aged with an accelerated stress test, respectively. They both observed inhomogeneous degradation along the stack. In particular, they found local

---

[*] Corresponding authors, michael.mo.obermaier@bmw.de, scheu@mpie.de

▲ *Paper presented at the 23rd EFCF Conference "Low-Temperature Fuel Cells, Electrolyzers, H2-Processing Forum" (EFCF2019), 2–5 July 2019 held in Lucerne, Switzerland. Organized by the European Fuel Cell Forum www.efcf.com*

variations in loss of electrochemical active surface area (ECSA) at different locations on single cells as well as on different cell locations within the stack [17, 18]. Nonetheless, none of them described degradation due to local fuel starvation, which is considered as a critical failure mode in automotive fuel cell applications [19–21]. The importance of this failure mode is emphasized by several studies experimentally investigating local fuel starvation on single cell level by simulating the degradation either by closing parts of the flow field channels [22, 23], impregnating the gas diffusion layer [24], reducing hydrogen stoichiometry [25, 26], supplying liquid water to the cell [27], or feeding air to the anode [28, 29]. Thinning and porosity loss of the cathode catalyst layer (CCL), an increase in the CCL's Pt particle size, and a loss of carbon at the CCL resulting in a performance loss of the cell are commonly found.

In this study both of the aforementioned highly relevant topics of automotive full size stack degradation analysis and local fuel starvation degradation obtained under realistic automotive conditions are addressed. The goal is to identify degradation phenomena with respect to their location on stack and cell level. Information about the distribution of degradation phenomena helps understanding different degradation process during fuel cell system operation and gives input to improve cell designs and operational strategies. Finally, a degradation mechanism for a novel degradation phenomenon is postulated.

2 Experimental

An automotive full size stack of the EU Inspire project, within the predevelopment stage was aged by applying conditions of different automotive driving points at a fuel cell test station for approximately 100 h. The stack as illustrated in Figure 1A, consists of more than 350 cells with an approximate active area of 300 cm^2 each. Gases, which were supplied in counter flow from one end of the stack, flow in an U-shape from manifold inlet to outlet. Cells from eight different positions along the stack (region 1 to 8 in Figure 1A) were investigated thoroughly, in order to depict degradation inhomogeneities. Extensive degradation analysis was performed by a systematic failure analysis approach in which various techniques were employed to capture defects on multiple length scales. The location of degradation phenomena on the MEA was described using a location matrix, as shown in Figure 1B.

Degradation analysis was initiated by photo documentation of bipolar plates, GDLs and CCMs. For CCM analysis, GDLs were carefully removed from the MEA.

Digital 3D-light microscopy (Keyence VHX-6000) was used to investigate the morphology of GDLs and CCMs. Panorama images were taken to get an overview of the degradation phenomena distribution. In addition, single images with different magnifications and light settings were taken to analyze different degradation phenomena. In order to reveal local degradation development on a single cell, images of every single segment of the location matrix (Figure 1B) were taken under the same conditions. A hole was artificially stamped into the MEA as a reference point in order to locally correlate degradation phenomena on GDLs, anode- and cathode catalyst layers. Keyence VHX-6000 software was used to determine 3D-dimensions of different degradation phenomena.

Scanning electron microscopy (SEM, FEI Quanta FEG 650) was applied to get deeper morphological information. Backscattered electrons (BSE) with an acceleration voltage of 5 kV were used in most cases for imaging. Secondary electrons were only used to visualize surface topography with an acceleration voltage between 1 kV to 2 kV.

To monitor the development of degradation like crack formation and Pt deposition within the location matrix (see Figure 1B) BSE images possessing a higher contrast than optical images were taken on different cells of the stack, thus supporting information obtained from optical microscopy. Depending on the degradation phenomena investigated, 9 to 20 SEM images under the same conditions were taken on every of the 6 selected cells.

For quantification of the aforementioned surface morphology changes image analysis of optical and SEM images was performed by manually applying a contrast threshold with the software Imagic IMS (Vers. V18Q4) to distinguishing different morphological compartments.

The surface area ratio of MPL adhesion on the catalyst layer was calculated as: area of MPL in image / total area of the image. The surface area ratio of cracks and Pt deposition was calculated as: area of cracks or Pt deposition in the image / area of MPL-free catalyst layer in the image. Regions of the CCL covered by the MPL were excluded from the analysis, as no information about crack formation or Pt deposition were accessible within these regions. It should be mentioned, that preferential formation of cracks or deposition of Pt in MPL-free areas of the CCL cannot
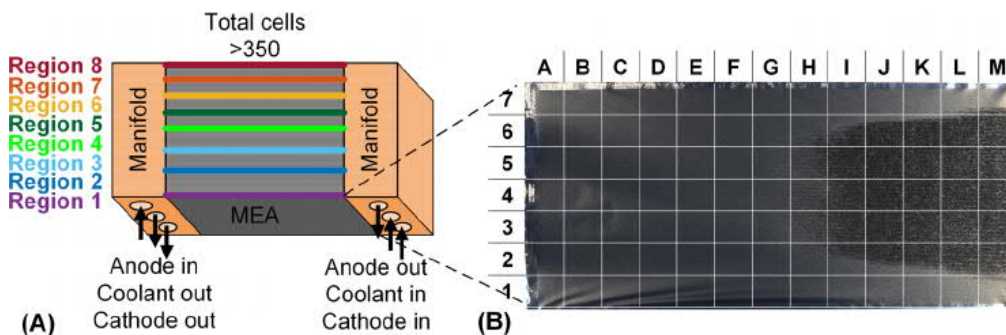

Fig. 1 (A) Schematic of an automotive full size stack indicating the location of cells under investigation. (B) Location matrix of the MEA placed on top of the CCL. The CCL shows increased microporous layer adhesion (dark region from H2 to M6) at the anode outlet.

be excluded. Following this hypothesis we cannot exclude an overestimation of the surface area ratio of cracks and Pt deposition with our calculation approach.

Cross sections of the active layers were prepared by a cryo cross section polisher (JEOL IB-19520CCP) to determine thickness or structural changes. The thickness of the single CCM layers being imaged with SEM (BSE, 5 kV) were again determined by image analysis with the help of the software GFaI Layers (Vers. 1.74). After selecting every single layer by manually setting a contrast threshold, roughly 60 single thickness measurements in a distance of 1 μm were automatically performed and averaged.

Energy dispersive X-ray spectroscopy (EDX, Oxford X-Max 50, 5–10 kV) was performed to identify different materials on and within the CCM during SEM measurements.

Finally, X-ray diffraction (XRD) (Bruker D8 Advance 2010) was applied to investigate Pt crystallite size changes. For qualitative comparison, Pt crystallite size was determined with Rietveld refinement under the fundamental parameter approach with the help of the software Bruker AXS Topas (Vers. 6).

3 Results and Discussion

3.1 Structural Changes of MEAs after Stack Operation

Investigation of degradation revealed distinct failure phenomena which were analyzed with respect to appearance and distribution on the active area and at different stack positions to obtain a comprehensive image.

GDLs of all investigated samples (15 MEAs at 8 different stack positions (see Figure 1A) showed increased adhesion towards the CCM compared to BOL samples, resulting in MPL adhering to the catalyst layer after MEA disassembly. It needs to be mentioned, that the GDL was not laminated onto the CCM during MEA production. On the anode catalyst layer (ACL) only minor MPL adhesion with a surface area ratio smaller 2% was observed. By contrast, we found strong MPL adhesion on the CCL (Figure 2A) having surface area ratios of up to 88% in a single segment of the location matrix. Optical microscopy revealed that adhesion of the MPL on the CCL was inhomogeneous and increased towards the anode outlet region (Figure 1B). Scanning electron microscopy images of CCM cross-sections in the region of strong

MPL adhesion showed a merging of the CCL and MPL at their interface.

Furthermore, cracks were visible in light and SEM micrographs (Figure 2B). The occurrence of cracks on the CCL strongly correlated with the regions of MPL adhering to the CCL. We found different typical crack shapes ranging from small crack networks, to linear cracks with radial side cracks, star like cracks as well as circular cracks. Six selected cells within region 1, 6, and 8 (Figure 1A) showed that the crack size and crack surface area ratio at the CCL increase towards the anode outlet region, as analyzed with image analysis. By contrast, only minor cracks at the ACL and no cracks on begin of life (BOL) samples (Figure 2C) were detected.

Besides cracks, the formation of a circular (Figures 3A and 3B) and a linear pattern (Figure 3C), which appeared bright in BSE micrographs (Figure 2B), were observed. Herein, circular deposition occurred both in a disc (filled ring) and ring like shape. The bright appearing features (Figures 2B and 3) were
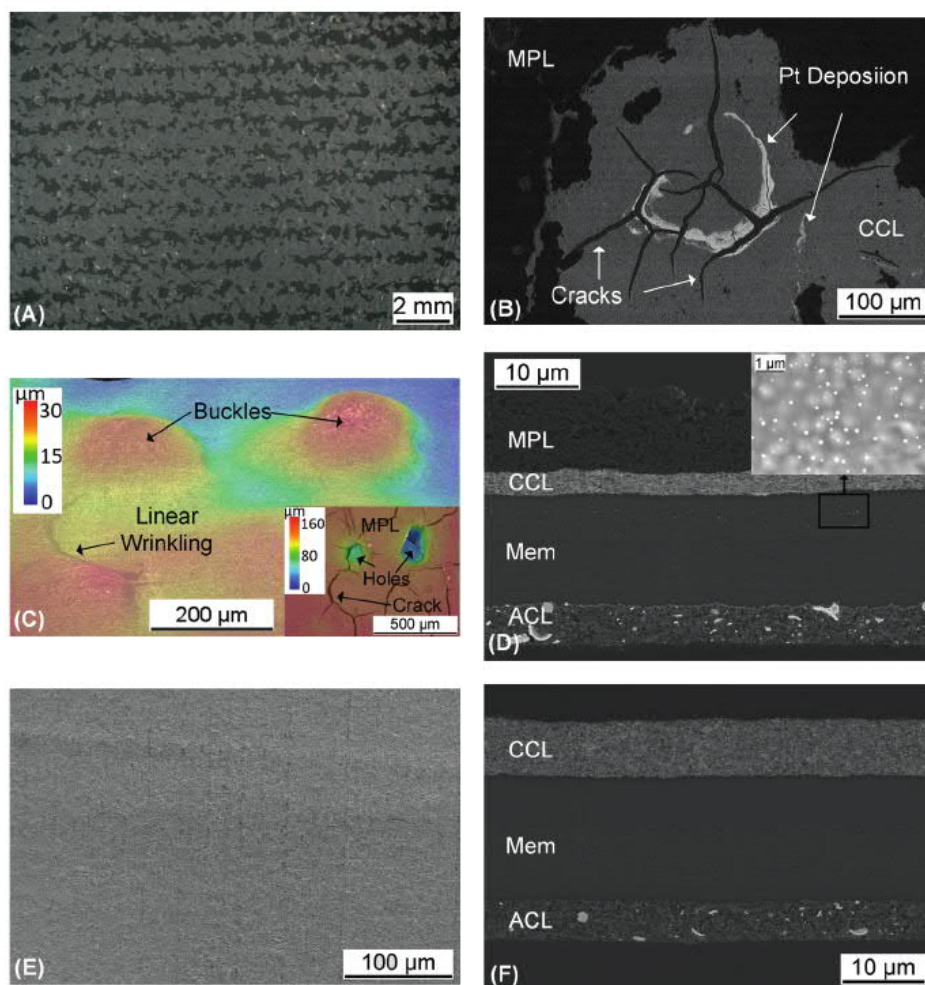

Fig. 2 Assembly of different degradation phenomena observed on the CCM: (A) Optical microscopy image of CCL (top-view) showing MPL adhesion (black) on CCL (gray). (B) SEM image of CCL (top-view) showing MPL adhesion (black), crack formation and circular and linear Pt deposition (white). (C) 3D-optical microscopy image showing buckling and linear wrinkling on the ACL. The inset shows corresponding holes and cracks in the MPL. (D) SEM image of CCM cross-section showing CCL layer thinning and formation of a Pt band close to the CCL. (E) SEM image of a BOL CCL (top-view). (F) SEM image of BOL CCM cross-section.

analyzed by EDX measurements and were shown to consist of Pt. This Pt deposition on top of the CCL appeared within regions of strong MPL adhesion. Optical panorama images showed cumulated occurrence of Pt deposition in distinct, but randomly distributed areas on the CCL close to the anode outlet. Threshold analysis of SEM images (taken from 4 cells of regions 6 and 8) showed a trend of increasing Pt deposition towards the anode outlet region. This result is supported by XRD measurements showing Pt crystallite growth towards the anode outlet region of the CCM. Compared to BOL samples we found an increase in crystallite size by approximately 33% ± 3% in the areas close to the anode inlet (values averaged of positions B2/B6) and of 115% ± 4% close to the anode outlet (values averaged of positions J3/J5) for a strongly degraded cell in region 6. For less degraded cells of region 7 we found an increase of Pt crystallite size by approximately 33% ± 2% in the areas close to the anode inlet (values averaged of positions B3/B5) and 54% ± 8% close to the anode outlet (values averaged of positions K3/K5) compared to BOL samples. Circular Pt deposition had a diameter range from a few tens micrometers to a few hundred micrometers while having a depth range from a few micrometers to a few tens micrometers.

Linear Pt deposition possessed an average width and height of a few micrometers while having an average length of a few hundred micrometers. Within its detection limits, SEM-EDX measurements of CCM cross-sections revealed that Pt concentration gradients did not exist in the proximity of the Pt deposition, neither in horizontal nor in vertical direction. Likewise, no change in catalyst layer porosity was found in the vicinity of the circular Pt deposition. In addition, 83% of 30 investigated circular Pt depositions also showed Pt deposition on the corresponding location of the MPL surface. The location of another 10% of these Pt depositions correlated to holes in the MPL, where Pt deposition could not definitely be proven. No Pt deposition was found on the ACL and BOL samples (Figure 2C).

Degradation due to carbon corrosion was shown by cross sections of CCM samples taken at different locations from anode inlet to outlet. As shown in Figure 4B, we observed a gradually decrease of the CCL thickness towards the anode outlet region in all regions of the stack. As shown in Figure 2E, in the region close to the anode outlet a collapse of the porous CCL structure was detected, compared to a BOL sample (Figure 2F). Within this region we observed a thickness decrease of up to 73% (region 1, Position L4, 2 cells investigated), 72% (region 6, Position L4, 2 cells investigated), and 64% (region 8, Position L4, 2 cells investigated) compared to
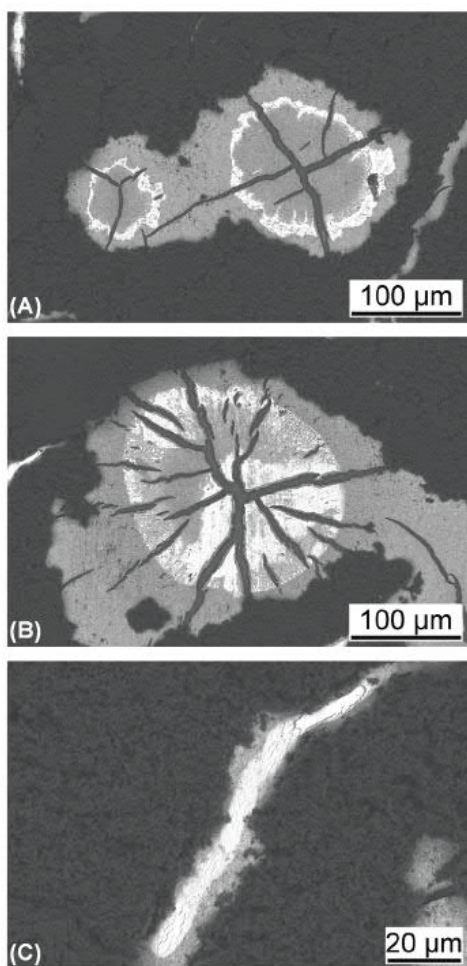

Fig. 3 Different types of macroscopic Pt depositions on top of the CCL imaged by SEM. (A) Ring-like Pt deposition. (B) Disc-like Pt deposition. (C) Linear Pt deposition.
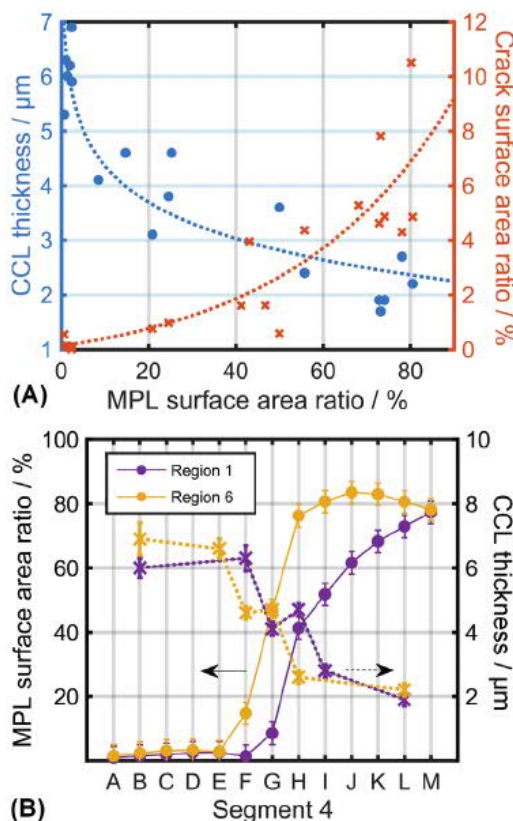

Fig. 4 (A) Correlation of surface area ratio of adhered MPL, CCL layer thickness (blue) and crack surface area ratio (orange) of different segments of 6 cells within stack region 1, 6 and 8. (B) Spatially resolved correlation of surface area ratio of adhered MPL (solid) and CCL thickness (dashed) along segment 4 (see Fig. 1(B)) of a single cell of region 1 (purple) and region 6 (yellow) of the stack.

BOL samples. ACL and membrane thickness remained constant within the measurement accuracy.

SEM-EDX measurements of CCM cross-sections also showed the formation of a Pt band in the membrane close to the CCL, whose intensity extended towards the anode outlet region.

Additionally, circular and linear protrusions and extrusions of the CCM (Figure 2D) were found on both the ACL and CCL. These circular and linear protrusions and extrusions, which will be referred to as buckling [30] and linear wrinkling, respectively, were observed to the same extent in terms of density and size distribution throughout all investigated single cells. Buckling exhibited a diameter range of a few tens micrometers to a few hundred micrometers, while having a height range of a few micrometers to a few tens micrometers. No differences of buckling at the anode and cathode were observed. Buckling was proven to be a wrinkling of the whole CCM by correlating location of protruding buckles at the CCL to extruding buckles at the ACL and *vice versa*. Buckling as a wrinkling of the whole CCM was also shown with cross-section images. Linear wrinkling possessed an average width and height of a few micrometers while having an average length of a few hundred micrometers. No correlation between linear wrinkling on the ACL and CCL could be found. As shown in the inset of Figure 2D, buckling and linear wrinkling were found to correlate to holes and cracks in the corresponding MPL by comparing their shape, size and position. Additionally, we discovered that 80% of 38 circular Pt depositions of a single cell in region 6 correlated with geometric displacements like buckling and linear wrinkling. Herein, the dimensions of 93% of 27 investigated Pt depositions were detected to be smaller than the dimensions of the corresponding buckle and linear wrinkling. No differences of buckling and linear wrinkling along a single cell and within different cells of the stack were observed.

3.2 Interpretation of Structural Changes

During operation MEAs undergo several relative humidity changes and can be exposed to harsh conditions like local fuel starvation, which can lead to the observed degradation phenomena. Especially, the observed degradation phenomena of CCL thinning, crack formation and Pt deposition indicate a rise of electrode potential at the cathode due to local fuel starvation [22–24, 28].

We expect elevated temperatures in the degraded area and carbon corrosion of the catalyst layer to be responsible for the adhesion of MPL and CCL. Agglomeration of ionomer on top of the CCL due to carbon corrosion in combination with an increased mobility of the ionomer due to increased temperature could lead to ionomer migration into the MPL and thus to the observed adhesion effect. In addition, carbon corrosion during fuel starvation could lead to a roughening of MPL and CCL surface, which could lead to a mechanical adhesion of the two layers.

We also assume carbon corrosion to support crack formation at the CCL due to a weakening of the CCL structure, thus leading to the increased crack surface area ratio at the CCL compared to the ACL. Crack formation itself is assumed to be caused by tensions within the catalyst layer originating from membrane swelling, which occurs during cycling of the relative humidity [30]. This is also in accordance with the preferential formation of cracks in the vicinity of CCM buckles, where CCM expands during buckle formation.

The fact that Pt deposition is accumulated in distinct but randomly distributed areas close to the anode outlet of the CCL leads to the assumption of water accumulation at the CCL surface being a prerequisite for Pt deposition. This hypothesis is in accordance with the relative position and shape of buckles and linear wrinkles on the CCM and holes and cracks in the MPL. For linear wrinkling no correlation on the ACL and CCL was found. Therefore, it might be a local wrinkling effect of the single catalyst layer, which is in accordance with the results of Mehmood et al. [32].

In accordance with the results of Uchiyama et al. [30, 31], buckling and linear wrinkling is supposed to occur due to relative humidity cycling of the cell during operation. While Uchiyama et al. simulated low supporting MPL areas by introducing a perforated foil between CCM and GDL to artificially create buckles, we observe buckling in a real system. Buckling formation is explained as follows: Due to relative humidity change the membrane swells and the CCM extends. At locations of low support due to holes or cracks in the MPL, the CCM releases the stress by wrinkling into these geometric displacements, thus forming buckles and linear wrinkles. This hypothesis is in accordance with the position and shape of buckles and linear wrinkles on the CCM in relation to holes and cracks in the MPL.

Linear wrinkling, where no correlation of linear wrinkles on the ACL and CCL was found, might be a local wrinkling effect of the single catalyst layer, which is in accordance with the results of Mehmood et al. [32].

3.3 Correlation of Fuel Starvation Degradation Phenomena

For simplification of further stack analysis related to fuel starvation we correlated the degradation phenomena of MPL adhesion, CCL thinning and crack formation being determined on different segments (along row 4) within 6 cells at stack position 1, 6, and 8. Figure 4A shows that an increase in MPL adhesion correlates with both an increase in crack surface area ratio as well as with a decrease in CCL thickness. In particular, Figure 4B shows strong CCL thinning in the transition region of low to high MPL adhesion of cells in region 1 and 7. In addition, we observed a correlation in terms of an increase in both MPL adhesion and Pt deposition towards the anode outlet region. Consequently, the degradation phenomena of MPL adhesion can be used as a first indicator for the degradation phenomena of CCL layer thinning, crack formation and to a certain extend Pt deposition. Therefore, our results allow the conclusion that a fast indication of fuel starvation degradation along different cells of the stack can be made by analyzing MPL adhesion on the single cells of the stack. It has to be mentioned that a transfer to different material systems and operation conditions still has to be proven.

3.4 Local Development of Degradation along Single Cells and within the Stack

In order to investigate the influence of cell geometry as well as cell stacking on degradation we used the aforementioned correlation of different degradation phenomena to perform a simplified stack degradation analysis. The representative degradation phenomena of MPL adhesion was quantified *via* calculation of MPL surface area ratio (as described in the experimental section) at various positions within a single cell. Quantification was repeated for cells at eight different stack positions (regions 1 to 8 in Figure 1A).

Figures 5A and 5B show the local development of the degradation along a single CCM at different stack positions. At

least two specimens were taken for each location to analyze the degradation phenomena. An exception was made for region 2, where only one cell was investigated. We found a general trend of increased MPL adhesion towards the anode outlet (position M7) in both horizontal (position A-M) and vertical direction (position 1–7). An exception was made for cells at the end of the stack (region 8), where we observed a decrease of MPL adhesion towards the anode outlet after an initial increase of degradation. This behavior might be due to a transport of excess hydrogen from the outlet manifold, which is also referred to as vacuum effect [33–35].

We also found local differences in total cell degradation according to the cell position within the stack. As shown in Figure 5C, we observed increased degradation, by means of MPL covering the CCL, in the middle of the stack slightly shifted to the end of the stack (region 4 to 6, where region 4 depicts the middle of the stack). In addition, slightly stronger degradation was observed in the region close to the stack inlet (region 1) and at the end of the stack (region 8). The distribution of degradation along the stack was in accordance with *in situ* data, showing cell voltages (at a current density of 1.4 A cm^{-2}) within regions of increased degradation being lower compared to cell voltages within other regions of the stack (see Figure 5C).

Due to the complexity of the automotive fuel cell system and its operating points a clear reason for the inhomogeneous stack degradation could not be found. However, the occurrence of regions of stronger degradation within the stack could be explained by stack and cell design as well as by self-reinforcing effects due to the mutual dependence of water accumulation and fuel starvation degradation. On the one hand, inhomogeneous incoming gas flow of different cells due to stack design and peripheral fuel cell system devices could have led to increased local fuel starvation in distinct cells. On the other hand, fuel starvation could have been supported by water accumulation within the MEA by preventing hydrogen to access the active area. The observed degradation of buckling and linear wrinkling are supposed to support the accumulation of water [32] on both anode and cathode. In addition, degradation phenomena like crack formation on top of the CCL could also lead to an enhanced accumulation of water on the cathode side [32, 36]. Due to water diffusion from cathode to anode, water accumulation at the anode could also be increased by the aforementioned cathode degradation. This could have led to a self-worsening effect of fuel starvation degradation supporting further fuel starvation. Therefore, both inhomogeneous incoming gas flow and the mutual dependence of water accumulation and fuel starvation can cause the observed inhomogeneous stack degradation.
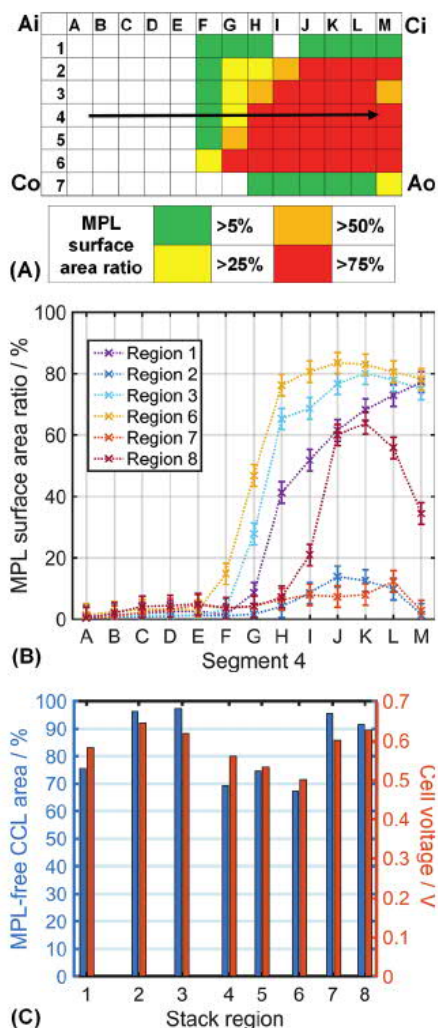

Fig. 5 (A) Distribution of MPL adhesion on an exemplary cell of the stack, showing increasing degradation from anode inlet to anode outlet. Ai/Ci and Ao/Co indicate positions of anode/cathode inlet and outlet, respectively. (B) Horizontal development of degradation from anode inlet to outlet region (as depicted by arrow in A) for different cells of the stack. Region 4 and 5 show similar results as region 6 and are excluded from the graph for reasons of clarity. (C) MPL free area of the CCL as a measure for cell degradation at different stack positions. Increased degradation (lower MPL free area) in the middle of the stack slightly shifted to the end of the stack (regions 4–6) as well as at both ends of the stack (regions 1 and 8) were observed. Cells with increased degradation showed lower performance in terms of *in situ* measured cell voltage.

3.5 Postulation of a Degradation Mechanism for Circular and Linear Pt Deposition

It is well agreed, that Pt agglomeration and particle growth is highly relevant for fuel cells and thus for stack performance loss [19, 37, 38]. Since circular and linear Pt deposition was observed throughout the stack and, to the best of our knowledge, has not

been described in literature yet, we tried to better understand this degradation mechanism. As illustrated in Figure 6, we assume voids between MPL and CCL like buckling and linear wrinkling of the CCM as well as MPL cracks and holes to be the starting point of degradation. At high current densities and/or high relative humidities of the supplied gases these voids at the cathode are suspected to be filled with liquid water. Additionally, due to possible hydrogen starvation at the anode, electrode potential U_c rises at the CCL according to the reverse current mechanism [28]. As a result of the increased cathode potential, Pt dissolves into water within the voids (Figure 6A) [39, 40]. The dissolution of Pt ions in water is supported by the results of Xie et al. [41]. When starved anode regions are resupplied with hydrogen the potential U_c of the CCL decreases and reaches the reduction potential of dissolved Pt ions, thus leading to deposition of the dissolved Pt (Figure 6B). In order to deposit Pt in the center of the macroscopic voids (diameter = few tens to few hundreds micrometers, depth = few to few tens micrometers), electrons have to migrate a long distance in the order of tens of micrometers within the strongly degraded cathode catalyst layer possessing a severe decreased thickness of approximately two to three micrometers. The large electric resistance of the long path electrons have to move within the collapsed electrode leads to an increase in electric potential towards the center of the void. Since the change of protonic potential from the edge to the center of the void can be neglected, the increase in electric poten-

tial leads to an increase in the local cathode potential (see Figure 6B). Thus, dissolved Pt will preferentially deposit at the edge of the water filled void, where a lower cathode potential is present (see Figure 6B). In addition, dissolved Pt ions will migrate towards the edges of the macroscopic void, due to the established electric field, also leading to increase Pt deposition at the edges of the void and thus explaining the formation of circular Pt deposition.

Another possible mechanism that could explain favored Pt deposition at the edges of the water filled void is given by cathode potential differences along the void during fuel starvation. According to the reverse current mechanism the potential increase at the cathode is caused by oxygen reduction reaction at the starved anode and thus dependent on the oxygen diffusion from cathode to anode. The water droplet within the void having a thickness of several micrometers and having an oxygen diffusion coefficient in the range of fully hydrated polymer-electrolyte membranes possesses an additional diffusion resistance for oxygen diffusion from cathode to anode. Thus, oxygen partial pressure at the anode and the corresponding local cathode potential in the center of the void is decreased. As a result, Pt dissolution at the edges of the water filled voids is enhanced leading to an increased Pt ion concentration in the water droplet in the proximity of the void's edges. This leads to an increased Pt deposition on top of the cathode catalyst layer compared to the center of the void, when the cathode potential drops below the Pt reduction potential during hydrogen resupply.

In case of linear Pt deposition, the width of a linear void (cracks; width = few micrometers, length = few hundred micrometers) is assumed to be not large enough to create a sufficient increase in electric potential and decrease in oxygen partial pressure. Thus, a linear Pt deposition is formed.

4 Conclusions

Different degradation phenomena were found on cells of an automotive full size stack operated under different automotive driving points. By correlating the observed degradation phenomena of crack formation, CCL thinning and Pt deposition, which are all related to local fuel starvation, to the degradation of MPL adhesion, a fast indicator for degradation inhomogeneities in particular for fuel starvation degradation within single cells and between different cells of the stack were presented. Buckling (wrinkling of the CCM) and linear wrinkling of the CL was observed continuously throughout the cell and stack, the other degradation phenomena were found to increase towards the anode outlet and exhibited different extent at different locations of the stack. An increased degradation in terms of MPL adhesion in the second half of the stack as well as a slightly increased degradation at both ends of the stack were detected. A potential rise at the CCL due to fuel starvation was assumed to be the main cause of degradation. Gas flow inhomogeneities and self-reinforcing effects due to the mutual dependence of water accumulation and fuel
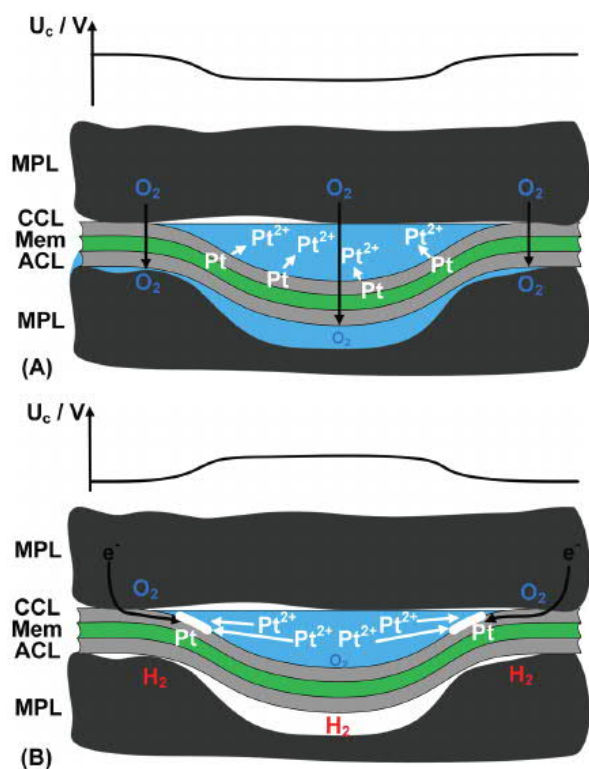

Fig. 6 Schematic of postulated formation mechanism of Pt deposition on top of the CCL. (A) Dissolution of Pt in water within a void (here: buckle) at elevated cathode potential due to local fuel starvation. (B) Pt deposition close to contact area of MPL/CCL (high current density for Pt-ion reduction) at reduced cathode potential.

starvation were thought to be responsible for the different extents of degradation along the stack. Finally a degradation mechanism for the formation of Pt deposition was proposed. In brief, voids between MPL and catalyst layer being filled with liquid water are suggested to be the starting point of the Pt deposition. A potential rise according to the reverse current mechanism is suggested to lead to Pt dissolution in water filled voids. After resupply of H_2 and corresponding decrease of potential, dissolved Pt deposits preferentially at the edge of water filled voids. This might be both due to increased cathode potential in the center of the void due to high in-plane electron resistance of the degraded CCM, and an increased Pt ion concentration at the edges of the water filled voids.

Acknowledgements

References

[1] International Transport Forum, (ITF 2017), *ITF Transport Outlook 2017*, OECD Publishing, Paris, France, **2017**, can be found under DOI: https://doi.org/10.1787/9789282108000-en.

[2] Shell Deutschland Oil GmbH, Shell Hydrogen Study, **2017**, can be found under https://www.shell.de/medien/shell-publikationen/shell-hydrogen-study/_jcr_content/par/toptasks_e705.stream/1497968967778/1c581c203c88bea74d07c3e3855cf8a4f90d587e/shell-hydrogen-study.pdf.

[3] United States Department of Energy (DOE), USA, Fuel Cell Technologies Office Multi-Year Research, Development, and Demonstration Plan, **2017**, can be found under https://www.energy.gov/sites/prod/files/2014/12/f19/fcto_myrdd_full_document.pdf.

[4] R. Lin, B. Li, Y. P. Hou, J. M. Ma, *International Journal of Hydrogen Energy* **2009**, *34*, 2369.

[5] S. R. Dhanushkodi, M. Schwager, D. Todd, W. Méridaa, *Journal of the Electrochemical Society* **2014**, *161*, 1315.

[6] M. Schulze, N. Wagner, T. Kaz, K. A. Friedrich, *Electrochimica Acta* **2007**, *52*, 2328.

[7] J. Shan, R. Lin, S. Xia, D. Liu, Q. Zhang, *International Journal of Hydrogen Energy* **2016**, *41*, 4239.

[8] N.-I. Kim, Y. Seo, K. B. Kim, N. Lee, J.-H. Lee, I. Song, H. Choi, J.-Y. Park, *Journal of Power Sources* **2014**, *253*, 90.

[9] L. Dubau, J. Durst, F. Maillard, M. Chatenet, J. André, E. Rossinot, *Fuel Cells* **2012**, *12*, 1888.

[10] G. de Moor, C. Bas, F. Lesage, A. S. Danérol, E. Claude, E. Rossinot, M. Paris, L. Flandin, N. D. Albérola, *J. Appl. Polym. Sci.* **2011**, *120*, 3501.

[11] Z. Luo, D. Li, H. Tang, M. Pan, R. Ruan, *International Journal of Hydrogen Energy* **2006**, *31*, 1831.

[12] P. Ferreira-Aparicio, A. M. Chaparro, B. Gallardo, M. A. Folgado, L. Daza, *ECS Transactions* **2010**, *26*, 257.

[13] F. Ettingshausen, J. Kleemann, A. Marcu, G. Toth, H. Fuess, C. Roth, *Fuel Cells* **2011**, *11*, 238.

[14] F. Nandjou, J.-P. Poirot-Crouvezier, M. Chandesris, J.-F. Blachot, C. Bonnaud, Y. Bultel, *Journal of Power Sources* **2016**, *326*, 182.

[15] L. Dubau, J. Durst, L. Castanheira, F. Maillard, A. Lamibrac, J. Dillet, G. Maranzana, O. Lottin, A. El Kaddouri, G. de Moor, C. Bas, L. Flandin, E. Rossinot, N. Caqué, M. Chatenet, *ECS Transactions* **2015**, *69*, 133.

[16] M. K. Cho, D.-N. Lee, Y.-Y. Kim, J. Han, H.-J. Kim, E. Cho, T.-H. Lim, D. Henkensmeier, S. J. Yoo, Y.-E. Sung, S. Park, J. H. Jang, *International Journal of Hydrogen Energy* **2014**, *39*, 16548.

[17] F. Ettingshausen, J. Kleemann, M. Michel, M. Quintus, H. Fuess, C. Roth, *Journal of Power Sources* **2009**, *194*, 899.

[18] P. Pei, X. Yuan, P. Chao, X. Wang, *International Journal of Hydrogen Energy* **2010**, *35*, 3147.

[19] R. Borup, J. Meyers, B. Pivovar, Y. S. Kim, R. Mukundan, N. Garland, D. Myers, M. Wilson, F. Garzon, D. Wood, P. Zelenay, K. More, K. Stroh, T. Zawodzinski, J. Boncella, J. E. McGrath, M. Inaba, K. Miyatake, M. Hori, K. Ota, Z. Ogumi, S. Miyata, A. Nishikata, Z. Siroma, Y. Uchimoto, K. Yasuda, K.-i. Kimijima, N. Iwashita, *Chemical Reviews* **2007**, *107*, 3904.

[20] P. Pei, H. Chen, *Applied Energy* **2014**, *125*, 60.

[21] N. Yousfi-Steiner, P. Mocotéguy, D. Candusso, D. Hissel, *Journal of Power Sources* **2009**, *194*, 130.

[22] R. N. Carter, B. K. Brady, K. Subramanian, T. Tighe, H. A. Gasteiger, *ECS Transactions* **2007**, 423.

[23] Z. Y. Liu, B. K. Brady, R. N. Carter, B. Litteer, M. Budinski, *Journal of the Electrochemical Society* **2008**, *155*, 979.

[24] T. W. Patterson, R. M. Darling, *Electrochem. Solid-State Lett.* **2006**, *9*, 183.

[25] D. Liang, Q. Shen, M. Hou, Z. Shao, B. Yi, *Journal of Power Sources* **2009**, *194*, 847.

[26] A. Taniguchi, T. Akita, K. Yasuda, Y. Miyazaki, *Journal of Power Sources* **2004**, *130*, 42.

[27] M. Kim, N. Jung, K. Eom, S. J. Yoo, J. Y. Kim, J. H. Jang, H.-J. Kim, B. K. Hong, E. Cho, *Journal of Power Sources* **2014**, *266*, 332.

[28] C. A. Reiser, L. Bregoli, T. W. Patterson, J. S. Yi, J. D. Yang, M. L. Perry, T. D. Jarvi, *Electrochem. Solid-State Letters* **2005**, *8*, 273.

[29] J. Kim, J. Lee, Y. Tak, *Journal of Power Sources* **2009**, *192*, 674.

ORIGINAL RESEARCH PAPER

[30] T. Uchiyama, H. Kumei, T. Yoshida, *Journal of Power Sources* **2013**, *238*, 403.

[31] T. Uchiyama, M. Kato, T. Yoshida, *Journal of Power Sources* **2012**, *206*, 37.

[32] A. Mehmood, M.-G. An, H. Y. Ha, *Applied Energy* **2014**, *129*, 346.

[33] D. Liang, M. Dou, M. Hou, Q. Shen, Z. Shao, B. Yi, *Journal of Power Sources* **2011**, *196*, 5595.

[34] Z. Liu, L. Yang, Z. Mao, W. Zhuge, Y. Zhang, L. Wang, *Journal of Power Sources* **2006**, *157*, 166.

[35] S. Kim, S. Shimpalee, J. W. van Zee, *Journal of Power Sources* **2004**, *135*, 110.

[36] F. E. Hizir, S. O. Ural, E. C. Kumbur, M. M. Mench, *Journal of Power Sources* **2010**, *195*, 3463.

[37] Y. Shao, G. Yin, Y. Gao, *Journal of Power Sources* **2007**, *171*, 558.

[38] M. F. Mathias, R. Makharia, H. A. Gasteiger, J. J. Conley, T. J. Fuller, C. J. Gittleman, S. S. Kocha, D. P. Miller, C. K. Mittelsteadt, T. Xie, S. G. Yan, P. T. Yu, *The Electrochemical Society Interface* **2005**, *Fall*, 24.

[39] A. A. Topalov, S. Cherevko, A. R. Zeradjanin, J. C. Meier, I. Katsounaros, K. J. J. Mayrhofer, *Chem. Sci.* **2014**, *5*, 631.

[40] X. Wang, R. Kumar, D. J. Myers, *Electrochemical and Solid-State Letters* **2006**, *9*, 225.

[41] J. Xie, D. L. Wood, D. M. Wayne, T. A. Zawodzinski, P. Atanassov, R. L. Borup, *Journal of the Electrochemical Society* **2005**, *152*, A104.